



CdS sensitized vertically aligned single crystal TiO₂ nanorods on transparent conducting glass with improved solar cell efficiency and stability using ZnS passivation layer

Shao-Hui Hsu^{a,b}, Sung-Fu Hung^a, Shu-Hua Chien^{a,b,*}

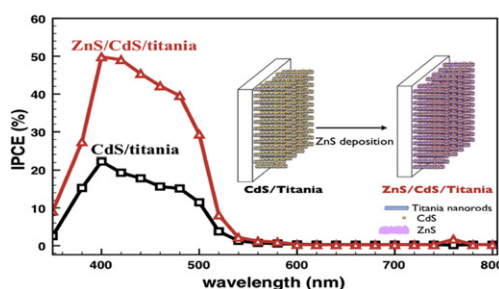
^a Institute of Chemistry, Academia Sinica, Taipei 11529, Taiwan

^b Department of Chemistry, National Taiwan University, Taipei 10617, Taiwan

HIGHLIGHTS

- The effect of ZnS amounts was studied in CdS-sensitized solar cell.
- ZnS was coated to prevent corrosion of the CdS and to facilitate photo-carriers transportation to TiO₂.
- The photo-to-electronic conversion efficiency is 1.84% which is one of the best efficiency in CdS/TiO₂ photoanodes.

GRAPHICAL ABSTRACT



ARTICLE INFO

Article history:

Received 23 August 2012

Received in revised form

10 November 2012

Accepted 16 January 2013

Available online 29 January 2013

Keywords:

Titanium oxide

Cadmium sulfide

Zinc sulfide

Nanorod

Passivation layer

Quantum dots-sensitized solar cell

ABSTRACT

Photoanodes consisting of CdS sensitized titania nanorods with ZnS passivation layer are applied for solar cells. Single crystal TiO₂ nanorods have been directly grown vertically on transparent conducting glass by a facile hydrothermal method and deposited with CdS and then a ZnS layer on the TiO₂ surface via a successive ionic layer adsorption and reaction (SILAR) method. The properties of ZnS/CdS/TiNR are characterized by XRD, SEM, TEM, UV–Vis, XPS, and electrochemical analysis. The effect of ZnS amount is studied in this system. Electrochemical results indicate the photocurrent density (J_{sc}) is greatly improved by increasing amount of ZnS. The incident photo-to-current conversion efficiency (IPCE), open-circuit voltage-decay (OCVD) method, and electrochemical impedance spectra (EIS) obviously substantiate these results. By optimizing the length of titania nanorods and the amount of CdS and ZnS, the best efficiency of 1.8% was achieved for solar cell under AM 1.5 G illumination with $J_{sc} = 4.19 \text{ mA cm}^{-2}$, $V_{oc} = 0.82 \text{ V}$ and FF = 54%.

© 2013 Elsevier B.V. All rights reserved.

1. Introduction

Titania (TiO₂) has attracted extensive attention for many applications such as photocatalysis [1], gas sensing [2], solar water splitting [3,4], lithium ion batteries [5,6], dye-sensitized solar cells

[7,8], and solid state dye-sensitized solar cells [9]. It is advantageous to employ nanostructured TiO₂ in solar cell applications due to its large surface area and appropriate conduction band position. One-dimensional (1D) TiO₂ materials including nanowires, nanorods, nanotubes, and nanotube arrays are currently of great interest owing to the possibility of establishing a direct electrical pathway which suppresses deleterious charge recombination. The typical methods to fabricate ordered 1D titania nanostructures for solar cell application include the template-assisted process [10,11] and

* Corresponding author. Institute of Chemistry, Academia Sinica, Taipei 11529, Taiwan. Tel.: +886 2 2789 8528; fax: +886 2 2783 1237.

E-mail address: chiensh@gate.sinica.edu.tw (S.-H. Chien).

anodization technique [12,13]. A conventional electrochemical anodization is a well-known approach to prepare self-ordering titania nanotubes array on any shape of titanium such as wire or foil. However, the titania nanotube arrays based solar cells were constructed in a back illuminated system and the performances of these devices decayed at least 25% by the losses at the electrolyte and the Pt counter electrode [14].

In order to avoid the above problem, front-side illumination is a better way for solar cell applications. It is challenging to directly grow aligned 1D TiO₂ structures on transparent conducting oxides (TCO) for photoanode. Template-assisted process has used to prepare one-dimensional TiO₂ micro structures on TCO by using ZnO nanowires [10] or anodic aluminum oxide (AAO) membrane [10] as a template. However, removing template is a tedious process. Recently, the fabrication of 1D TiO₂ nanostructures on conducting substrates have been reported [15–18]. The transparent titania nanotube array on TCO substrate with length between 0.3 μm and 33.0 μm was prepared by a electrochemical approach, including deposition of metal film and then anodization on the TCO [15]. Rutile TiO₂ nanowire arrays up to 5 μm long on TCO were fabricated via a non-polar solvent/hydrophilic substrate interfacial reaction under mild hydrothermal conditions [16]. In our group, the open-ended anodic TiO₂ nanotube films were obtained through anodization of Ti foil, wet-chemical etching and adherence on the transparent conducting oxide glass [17]. Aydil et al. used a hydrothermal method to grow oriented single-crystalline rutile TiO₂ nanorod array on fluorine-doped tin oxide (FTO) [18].

Many groups have recently reported quantum dots-sensitized solar cells owing to the well-defined synthesis of quantum dots with tunable size that results in the possibility of multiple excitons from single photon absorption [19–26]. Cadmium sulfide (CdS) is used as sensitizer because its narrow bandgap (2.42 eV) enables light harvesting in the visible light region. Numerous methods to deposit CdS on TiO₂ surfaces have been reported, including SILAR method [27], single-step electrodeposition [28], and modified electrochemical atomic layer deposition [29]. CdS modified TiO₂ is often used as photoanode materials for solar cells. In 2007, Chang and Lee developed a CdS quantum-dots-sensitized solar cell prepared by depositing CdS quantum dots onto 5.5 μm mesoscopic TiO₂ films and its efficiency was as high as 1.8% [20]. In 2010, an efficiency of 1.1% was achieved by co-sensitizers on oriented single-crystalline TiO₂ nanowire array using CdS and CdSe [24]. Noteworthy, the corrosion problem of narrow bandgap semiconductors in this type of solar cells still needs to overcome. In the past, a barrier layer of ZnS deposited onto the CdS surface was reported in order to enhance the stability of quantum dots sensitized solar cell, to inhibit the corrosion of CdS, and to prevent the recombination of injected electrons with holes in the electrolyte [19]. However, the quantitative effect of ZnS passivation layer on the cell performance has not been studied. In this study, we prepared single crystal TiO₂ nanorods directly on FTO by using a facile hydrothermal synthesis at 130 °C. Using SILAR method, CdS and ZnS were subsequently deposited on the TiO₂ nanorods as sensitizer and passivation layer, respectively. The effect of ZnS amount on the resultant photovoltaic measurement was investigated through electrochemical experiments. The ZnS/CdS sensitized rutile titania nanorod structure was used as photoanode of solar cell. Herein, the best efficiency, 1.8%, is one of the highest reported for CdS sensitized titania nanostructures.

2. Experimental

2.1. Preparation of titania nanorods on TCO

Oriented titania nanorods (TiNR) were prepared by the hydrothermal method as Andil et. al [18]. The precursor solution was

mixed with the de-ionized water (40 mL) and concentrated hydrochloric acid (40 mL, HCl, 37%, MERCK) and added 1.3 mL of tetra-n-butyl orthotitanate (TBOT, $\geq 98\%$, MERCK) with stirring for 15 min. The FTO glass (F:SnO₂, Uniregion Bio-tech, 7 Ω) were put vertically in the precursor solution and sealed in a Teflon-lined autoclave that was placed in an electronic oven at 130 °C for 20 h. After cooling to room temperature, the TiO₂ on FTO glass was rinsed with de-ionized water and dried at room temperature, denoted as 1TiNR. Repeating the hydrothermal process by using a fresh solution would lead to a thicker TiO₂ film thickness. In the present study, two other samples, 2TiNR and 3TiNR, were prepared, according to two or three repeating times of hydrothermal process.

2.2. CdS deposition

The precursors used in this investigation to prepare CdS were cadmium nitrate tetrahydrate (Cd(NO₃)₂ · 4H₂O, Alfa Aesar, 98.5%) and sodium sulfide nonahydrate (Na₂S · 9H₂O, Alfa Aesar, 98%). CdS was deposited on the above prepared TiNR using SILAR method. Subsequently, the TiNR samples were immersed in 0.5 M Cd(NO₃)₂ ethanol solution and immediately dipped into 0.5 M Na₂S ethanol solution. The above mentioned dipping steps were called one SILAR cycle. As the desired sample was obtained, it was calcined at 450 °C for 30 min in an argon stream.

2.3. ZnS and ZnO passivation layer treatment

The ZnS passivation layer onto CdS/TiNR surface was formed by using SILAR with ZnAc₂ (0.1 M) (Zinc acetate, J. T. Baker, 100%) and Na₂S (0.1 M) aqueous solutions via SILAR method. The CdS/TiNR was immersed in the ZnAc₂ and Na₂S aqueous solution subsequently. The resulted sample was denoted as xZnS/yCdS/zTiNR. The value of x, y, and z is corresponding to ZnS deposited cycle, CdS deposited cycle, and the repeating times of hydrothermal process of TiNR formation. A list of abbreviations and nomenclature is list in the Supporting information 1. For comparison study, deposition of ZnO passivation layer was carried out by dipping 0.1 M Zn(NH₃)₄ aqueous solution and hot water (95 °C) via SILAR method.

2.4. Preparation of CdS-sensitized solar cells

The obtained ZnS/CdS/TiNR samples were used as working electrodes in CdS sensitized solar cells. The counter electrode was a platinum-coated FTO substrate which is prepared by sputtering. The solar cell device was prepared by infiltrating between ZnS/CdS/TiNR and Pt counter electrode with iodide based electrolyte solution containing 0.5 M LiI, 0.05 M I₂, and 0.5 M *tert*-butylpyridine in anhydrous acetonitrile. Electrode spacing between the working and counter electrodes was ensured by the use of a 60 μm thick spacer (Capton, 3 M), leaving a window of area of 0.25 cm² as working electrode.

2.5. Characterization

The powder X-ray diffraction (XRD) patterns were recorded on a Philips X'pert with copper K α radiation ($\lambda = 1.5406 \text{ \AA}$) over angles from 20 to 80°. A scanning rate of 5° per minute was applied in all XRD experiments. Field emission scanning electron microscopy (FE-SEM) images were obtained on a JSM 6500F (JEOL). Transmission electron microscopy (TEM) image, high resolution transmission electron microscopy (HR-TEM) image, and selected area electron diffraction (SAED) result were obtained with a Tecnai G2 F20 (Philips), operating at an acceleration voltage of 200 kV. A spectrophotometer (Hitachi, U-3310) was used to record the UV–Vis spectra in the range 400–800 nm. X-Ray photoelectron

spectroscopy (XPS) was performed on a Omicron ESCA spectrometer using Al-monochromatic X-ray. The pressure of the analyzer chamber was maintained below 1×10^{-10} torr during the measurement. The binding energy was calibrated using the C 1s photoelectron peak at 284.5 eV as reference.

2.6. Photovoltaic measurements

Photoelectrochemical experiments were performed using an electrochemical analyzer (650B, CH Instruments) and devices were illuminated with a calibrated AM 1.5 solar light simulator (Oriel Class A Solar Simulators, Model: 91195A) operating at an intensity of 100 mW cm^{-2} . The light intensity was adjusted with a monocrystalline Si reference cell. The current density–voltage measurements (J – V) were conducted through a voltage range from 0 V to 1 V with illumination. The open circuit potential (V_{OC}), short circuit current density (J_{SC}), fill factor (FF) and energy conversion efficiency (η) were obtained. The current density–time measurements (J – t) were performed with or without light source and the data were collected by electrochemical analyzer and recorded in the computer. The incident photon-to-current conversion efficiency (IPCE) experiments were carried out using the system which contained a Xe lamp (300 W) with a monochromator (Oriel 74100). The light intensity was measured with an optical power meter (Ophir Optronics 70310) equipped with a calibrated thermopile head (Ophir Optronics 71964). The open-circuit voltage decay (OCVD) measurements were employed to study the electron recombination kinetics. The solar cell device was illuminated for 5 s using an AM 1.5G simulated light and the voltage decay was measured after switching off the light. The electrochemical impedance spectroscopy (EIS) measurements were performed by applying a frequency range from 0.1 to 10^5 Hz with AC amplitude of 10 mV in the dark at an applied voltage of 0.7 V or under illumination at open-circuit voltage.

3. Results and discussion

3.1. Characterization of photoanodes

Fig. 1a and b show the top-view and the side-view FESEM images of TiNR. The top-view FESEM image indicates that the entire FTO substrate is covered with a uniform high density titania nanorods with 150 nm in the average diameter and 1 μm in length. The average diameters of 2TiNR and 3TiNR are 240 nm and 500 nm; the average lengths are 2 μm and 3 μm , respectively. The FESEM images (Fig. 1c and d) of 5CdS/2TiNR show that the CdS nanoparticles are deposited on the surface of titania nanorods. It is indicated that Cd^{2+} and S^{2-} ions are able to diffuse to the bottom of the nanorods to form the desired CdS nanocrystallites. The FESEM images of 8ZnS/5CdS/2TiNR show that ZnS forms a thin layer nanostructure on the surface of samples. The energy dispersive X-ray spectroscopy (EDX) shows atomic composition of Zn is 0%, 1.0% and 1.8% on 5CdS/2TiNR, 2ZnS/5CdS/2TiNR and 8ZnS/5CdS/2TiNR, respectively.

Fig. 2 shows the XRD profiles of the FTO substrate, the titania nanorods, and CdS/TiNR. As compared to the tetragonal rutile phase of TiO_2 (SG, $P4_2/\text{mmn}$, JCPDS No. 88-1175, $a = b = 0.355 \text{ nm}$ and $c = 0.449 \text{ nm}$), the XRD patterns of TiNR reveal a significantly enhanced (101) and (002) peaks, indicating that highly oriented titania nanorods were grown vertically on the FTO surface. The TiO_2 nanorods grow along the [001] direction that is perpendicular to the FTO surface. Some diffraction peaks including (110) and (211), which are present in polycrystalline TiO_2 powder, are absent due to the highly aligned nanorods. The CdS/TiNR XRD pattern shows the presence of the hexagonal wurtzite phase of CdS (JCPDS No. 41-1049). The high resolution transmission electron microscopy (HRTEM) image, shown in Fig. 3a, also reveals completely crystalline TiO_2 nanorods grow along the [001] direction, consisting with the XRD results, with lattice spacing of $d = 3.2 \pm 0.1 \text{ \AA}$. The SAED pattern of a single nanorod along the [010] zone axis (Fig. 3b)

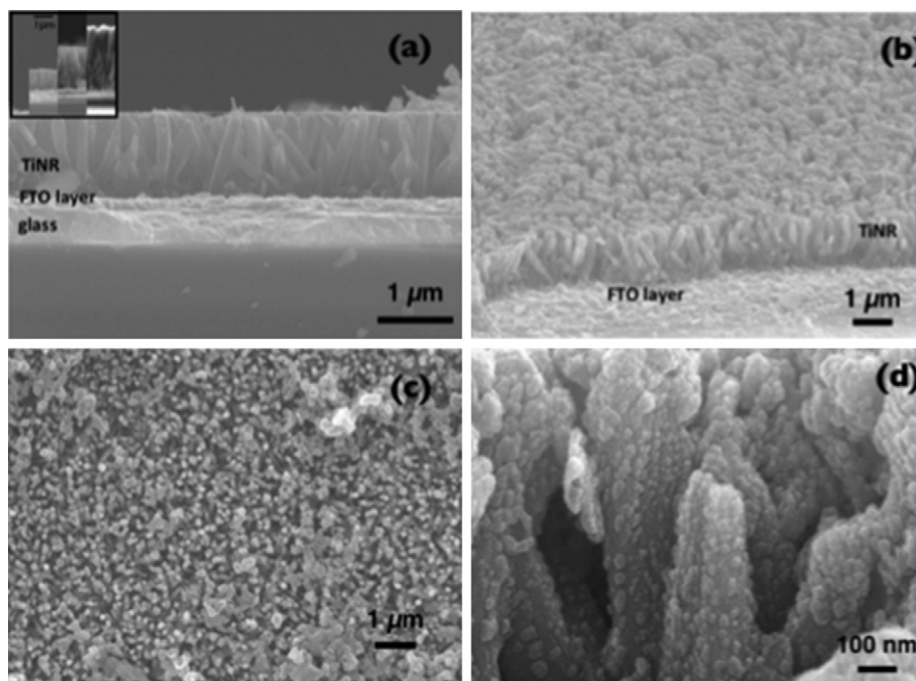


Fig. 1. The FESEM images of titania nanorods film on FTO substrate and CdS sensitized titania nanorods film: (a) side view, (b) tilted cross-section view of TiNR, (c) top view of 5CdS/2TiNR and (d) side view of 5CdS/2TiNR. Inset shows the cross-sectional view of the TiNR under various times of hydrothermal process. When hydrothermal process cycle (equals to 1, 2 and 3) was finished, the nanorod lengths were observed nearly 1, 2 and 3 μm , respectively.

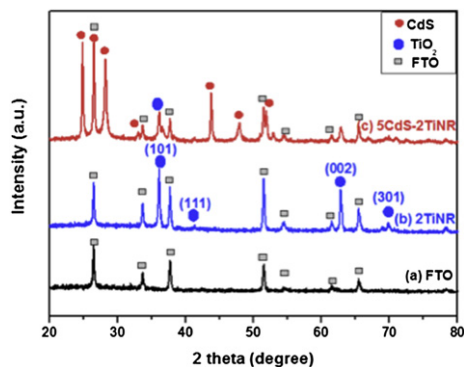


Fig. 2. The X-ray diffraction patterns of (a) FTO substrate, (b) titania nanorods on the FTO and (c) CdS deposited TiNR.

reveals single-crystallinity of TiNR. In Fig. 3c, the HRTEM image of CdS/TiNR clearly displays CdS nanoparticles with lattice spacing of $d = 3.2 \pm 0.1$ Å, corresponding to (101) plane in hexagonal CdS. The adjacent distance between the two semiconductors, formed by ions adsorbing, is a considerable criterion for achieving efficient charge separation under suitable corresponding band positions [23].

The UV–Vis spectrum as shown in Fig. 4 reveals that bare titania nanorods have no absorption in the visible region. Compared to the bare TiO₂ nanorod, all samples containing CdS display absorption extends to 540 nm due to the narrow bandgap (~ 2.42 eV) of the semiconductor. The absorption band edge of the yCdS/TiNR films occurs at 540 nm, 550 nm and 560 nm, respectively. Furthermore, for a series of CdS deposited TiNR films, the absorbance increases with CdS SILAR cycles, indicating the increased amounts of CdS nanocrystallites.

Fig. 5 exhibits the XPS spectra of CdS/TiNR with or without ZnS passivation layer. The binding energy of 284.5 eV for carbon 1s was used as internal reference. The Zn 2p doublet signals at 1021.7 eV and 1044.8 eV appear in ZnS/CdS/TiNR as shown in Fig. 5a. The

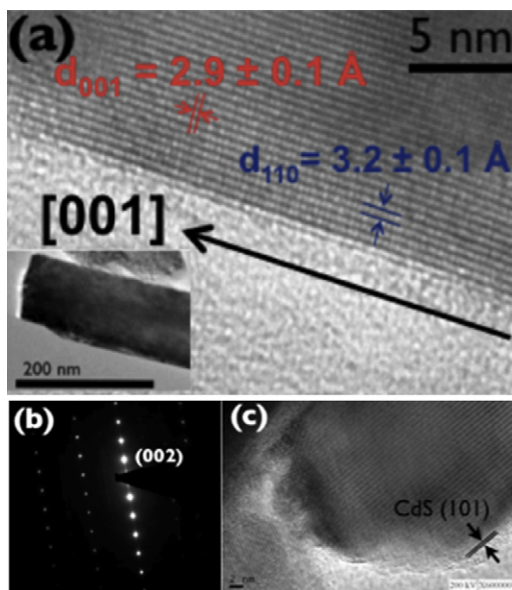


Fig. 3. The HRTEM images of titania nanorods and CdS/TiNR. The images and SAED of titania nanorods are shown in the figure (a) and (b). The d-spacing of plane (001) and (110) of titania nanorod with rutile phase are recorded as 2.9 ± 0.1 Å and 3.2 ± 0.1 Å, respectively. The SAED image reveals that titania nanorods are single crystalline. CdS nanocrystallites are deposited on the surface of titania nanorod with d-spacing of plane (101) is 3.2 ± 0.1 Å corresponding to JCPDS 41-1049.

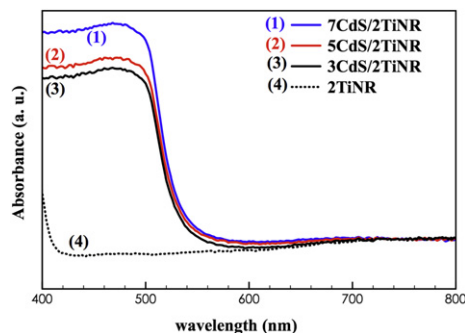


Fig. 4. The UV–Vis spectrum of 3CdS/2TiNR, 5CdS/2TiNR and 7CdS/2TiNR.

intensity of Cd 3d is significantly reduced in ZnS/CdS/TiNR as compared with CdS/TiNR in the Fig. 5b. While the S 2p doublet signals at 161.0 and 162.0 eV appear for both samples, the higher intensity of ZnS/CdS/TiNR is observed. The coverage of ZnS on the CdS/TiNR surface is evident.

3.2. Photovoltaic measurements

3.2.1. Effect of ZnS as passivation layer

CdS quantum dots would be easily corroded in solar cell system owing to solar light illumination [30,31] or interaction with electrolyte [32]. To avoid photocorrosion of the CdS nanoparticles, a wide bandgap semiconducting material commonly used for passivation of the surface of narrow bandgap quantum dots. In this part, the various amount of high bandgap semiconductor, ZnS (bandgap is 3.8 eV), was deposited on CdS/TiNR as protection layers via a facile SILAR approach. As the ZnS/CdS/TiNR samples were used as photoanodes for solar cells, current density–time measurements ($J-t$) of 5CdS/1TiNR with various amount of ZnS were carried out. The results are shown in Fig. 6a. The photocurrent density under illumination increases with increasing ZnS content. The resulted currents densities are 1.72, 1.86, 2.71, 2.98, 4.38 and 1.76 mA cm⁻² for xZnS/5CdS/1TiNR with x equal to 0, 2, 4, 6, 8 and 10, respectively. Compared to bare CdS/TiNR without ZnS passivation layer, the initial photocurrent density of 8ZnS/5CdS/1TiNR is enhanced by about 150% and remains unchanged during 60 s. This indicates that the CdS retains their activity when passivated with a ZnS layer. However, significant decrease in the photocurrent density decreases was recorded in the 10ZnS/5CdS/2TiNR sample. It might be due to the interruption of the hole transport pathway by the thicker ZnS layer. ZnS passivation layer was considered not only avoiding CdS photocorrosion but also protecting chemical corrosion from iodide based electrolyte [23–25]. In the present study, we also examine ZnO passivation layer of 5CdS/1TiNR to reduce the corrosion phenomenon. The results of $J-t$ experiments of ZnO/CdS/TiNR are shown in the Fig. 6b. The initial current density of 1.42 mA cm⁻² in the experiment is slightly lower than that of the unpassivated CdS/TiNR. The current density decays to 1.29 mA cm⁻², nearly 9% during 60 s. It means that the cell stability of ZnO/CdS/TiNR is poorer according to the $J-t$ experiment. The lower photocurrent density of ZnO passivated CdS/TiNR solar cell is attributed to the electrons transportation via two possible electron pathways, from CdS to titania nanorods or zinc oxide, in ZnO/CdS/TiNR solar cell owing to the similar bandgap and band position of ZnO and TiO₂. The illustrations of band diagram of two kinds of solar cells are shown in Fig. 7. As the photo-electrons and holes through the absorption of light in the narrow bandgap semiconductor CdS are generated, the photoelectrons subsequently transport to the conduction band of TiO₂, and then they are

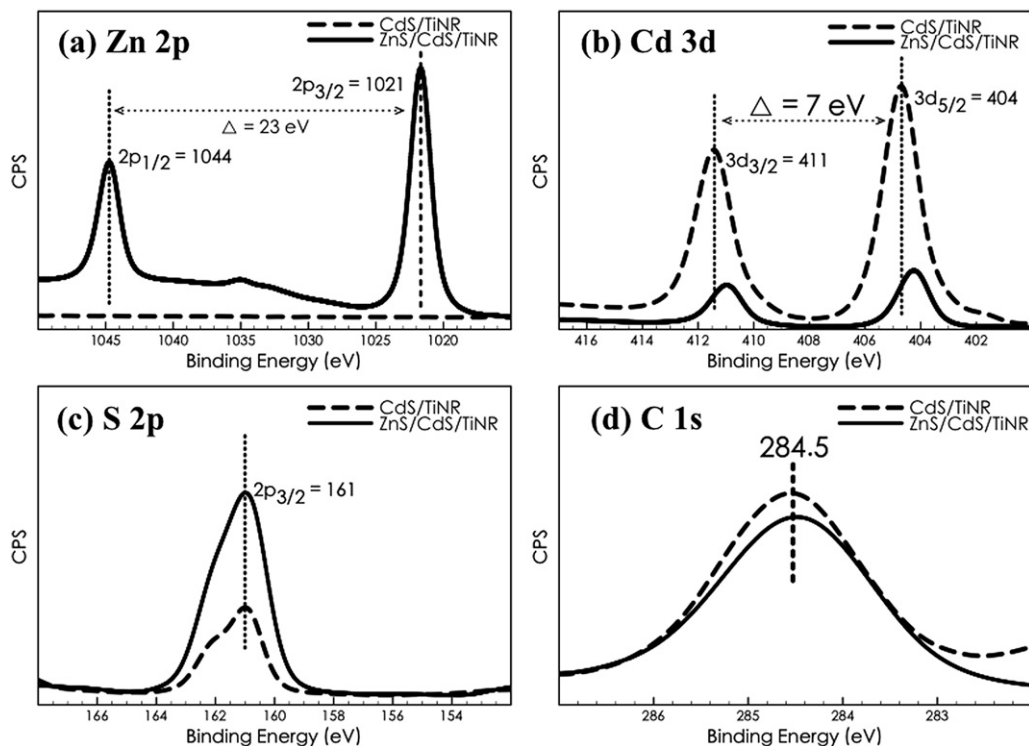


Fig. 5. The XPS spectra of CdS/TiNR with or without ZnS passivation layer: Zn 2p (a), Cd 2p (b), S 2p (c) and C 2s (d), respectively.

collected by electrochemical analyzer in the case of ZnS/CdS/TiNR. In the case of ZnO/CdS/TiNR, the photoelectrons might transport to conduction band of titania nanorods as well as ZnO layer. It provides an evidence that passivation layer not only avoids the corrosion effect of CdS from the photon or the electrolyte but also facilitates the transportation and collection of excited electrons. The measured cell performances with various deposition amount of ZnS are depicted in Fig. 8a and the related parameters are summarized in Table 1. All the short-circuit photocurrent and solar conversion efficiency increase with increasing ZnS deposition up to 8 cycles of SILAR. The open circuit potential with 10ZnS/5CdS/2TiNR exhibited the highest value of 0.83 V, which is remarkably larger than the V_{OC} of the electrode without ZnS. The higher V_{OC} with relatively thicker ZnS passivation layer in the electrode is due to the Fermi-level alignment of ZnS/CdS composition. It is noteworthy that 8ZnS/5CdS/2TiNR exhibits superior short-circuit photocurrent and efficiency (4.19 mA cm^{-2} , 1.8%) as compared to that without ZnS in the electrode. The IPCE measurements provide more

photo-response evidence of the effect of ZnS. IPCE values, as shown in Fig. 8b, are calculated from the following equation, $\text{IPCE} = (1240 \times J_{SC})/(\lambda \times P_{in})$, where λ and P_{in} are incident photon wavelength and incident power, respectively. All the photoanodes with deposit ZnS show an enhanced in %IPCE in the range of 350–500 nm (Fig. 8b). This enhancement is attributed to the passivation effect of ZnS. However, the further increasing in amount of ZnS, as in the 10ZnS/5CdS/2TiNR cell, it shows a remarkable decrease in the %IPCE. This is due to the obstruction effect on the hole transport. Higher %IPCE causes higher photocurrent density and better cell efficiency. The %IPCE in 8ZnS/5CdS/2TiNR is as high as 40–50% in the wavelength range of 400–500 nm and has magnitude up to 560 nm, consisting with the result of UV–Visible spectrum. At 400 nm, IPCE of 8ZnS/5CdS/2TiNR is 50% that is 2.2 times that of CdS/2TiNR and 1.6 times that of 2ZnS/5CdS/2TiNR. The recombination kinetics was examined by measuring the open-circuit voltage-decay (OCVD) method. The OCVD method is a way to probe the kinetics of recombination during the relaxation from illuminated

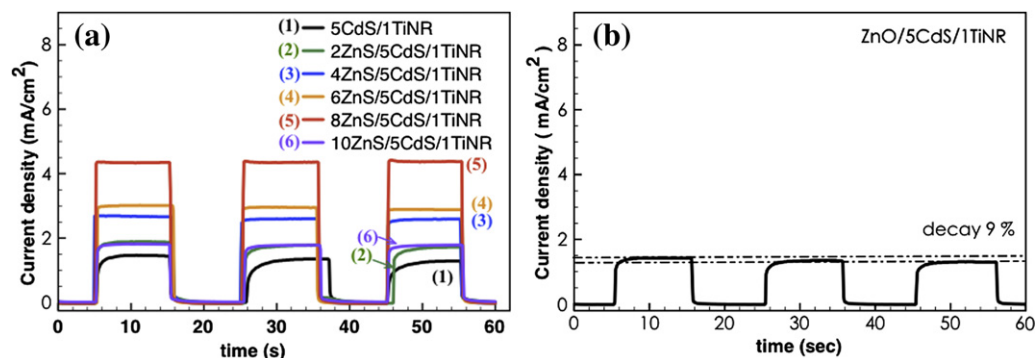


Fig. 6. The results of current density to time measurement of 5CdS/1TiNR with different ZnS deposited cycles (a) and ZnO/CdS/TiNR.

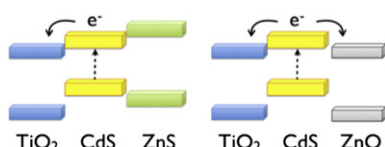


Fig. 7. Band edge structure for efficient transport of the excited electrons in CdS/TiNR with ZnS or ZnOg passivation layer.

quasi-equilibrium state to the dark equilibrium. Basically, OCVD is a dark measurement of the solar cell and hence only recombination to the electrolyte is measured. The electron lifetime is obtained by the reciprocal of the derivative of the decay curve normalized by the thermal voltage: [33]

$$\tau_n = -\frac{k_B T}{e} \left(\frac{dV_{OC}}{dt} \right)^{-1} \quad (1)$$

where τ_n is the electron lifetime that is a function of open-circuit photovoltage, V_{OC} ; $k_B T/e$ is the potential of thermal energy, and $(dV_{OC}/dt)^{-1}$ is the reciprocal of the instantaneous slope of $V-t$ curve. The results of V_{OC} decay are shown in Fig. 8c and the resulting lifetimes are depicted in Fig. 8d. According to the curves, three distinct regions are observed, which correspond to the three types of recombination mechanisms. The phenomenon is in agreement with the previous report [33]. At very initial decay in the high voltage, four curves display the same slope. It indicates that the lifetime of free electrons in the conduction band is a constant and is not affected by the interference of surface traps. At the middle voltage part, the response time is in the log-linear representation. The slower V_{OC} decay in 8ZnS/5CdS/2TiNR is observed that corresponds to the longer lifetime. In this region, charge transfer is dominated by the conduction band states and the response time depends on the process of trapping and thermal de-

Table 1

The kinetic parameters obtained from the EIS analysis. (Fitting was performed with z-view software. The symbols, L , k_{eff} , τ , R_k , R_w , D_{eff} , and n_s are the thickness of TiNR, first-order reaction constant, electron lifetime, charge transfer resistance related to recombination of electrons, interface transfer resistance, effective diffusion coefficient, and electron density per unit volume, respectively.

	L (μm)	k_{eff} (s^{-1})	τ (ms)	R_k (ohm)	R_w (ohm)	D_{eff} ($1 \times 10^{-5} \text{ cm}^2 \text{ s}^{-1}$)	n_s ($1 \times 10^{18} \text{ cm}^{-3}$)
5CdS/2TiNR	2	123.0	1.3	31.7	5.6	2.79	1.65
2ZnS/5CdS/2TiNR	2	122.5	1.3	54.3	4.5	5.59	2.07
8ZnS/5CdS/2TiNR	2	69.75	2.3	72.2	2.2	9.19	4.23
10ZnS/5CdS/2TiNR	2	150.6	1.0	47.0	4.5	6.35	2.08

trapping through the conduction band. It is a direct evidence of the passivation effect of ZnS due to the reduced recombination. At low voltage, electrons transport in traps after thermal de-trapping to the conduction band and re-capture by the surface trap. However, as the CdS/TiNR surface is covered with thicker ZnS layer, such as 10ZnS, the recombination process changes from a preferential recombination with the electrolyte to the preferential recombination with the CdS [34]. An additional proof was obtained from the electrochemical impedance spectroscopy in the dark condition in which the recombination only due to the influence of electrolyte. The Nyquist plots of cells with various deposit ZnS amount are shown in the Supplementary information 2. One semicircles was observed in the Nyquist plot and the middle-frequency area is attributed to the charge transfer resistance at the interface of TiNR/CdS/ZnS/electrolyte. The radius of the semicircle in the 8ZnS/5CdS/2TiNR is larger, indicating that the recombination resistance, R_r , is higher than others. The electron lifetime of each ZnS/CdS/TiNR cell that determined the minimum frequency of mid-frequency peak is obtained. The electron lifetime from dark EIS analysis exhibits the

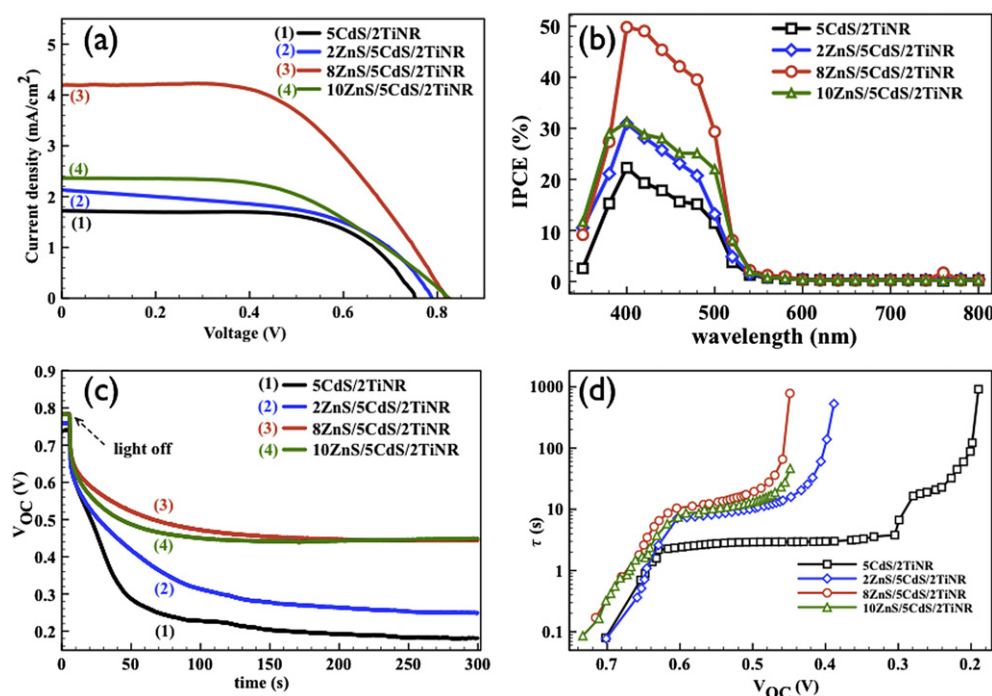


Fig. 8. The characteristics of solar cells with various the lengths of the titania nanorods, the CdS sensitizer content and the thickness of the ZnS passivation layer. (a) $J-V$ characteristics of 5CdS/2TiNR with various ZnS passivation layer thickness. (b) Incident photon to current conversion efficiency of 5CdS/2TiNR with different ZnS amounts (c) OCVD measurement of cells. (d) resulting electron lifetime under various voltage by OCVD.

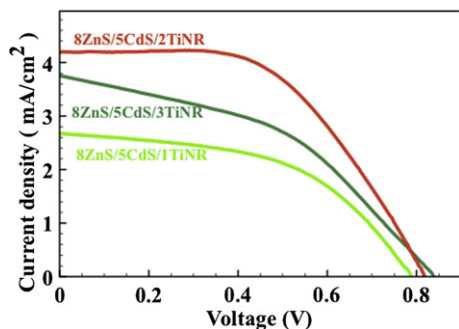


Fig. 9. Dependence of the J – V characteristics on the various TiNR length.

highest value of 0.163 s in 8ZnS/5CdS/2TiNR from EIS analysis at 0.7 V. Both OCVD and EIS measurements were carried out in dark condition and the similar results of electron lifetime are obtained. The results of OCVD and EIS further supports a better electron transport in the photoanode by suppressing the recombination at the photoanode/electrolyte interface. The EIS under solar light illumination was also used to investigate the recombination of excited electrons at electrolyte/electrode and CdS/TiO₂ interface as well as in CdS. The Nyquist plots under illumination are depicted in the [Supplementary information 3](#). The data were fitted in terms of the appropriate equivalent circuit suggested by Adachi et al. [35] and the calculated kinetics parameters were summarized in the [Table 1](#). The higher value effective diffusion coefficient (D_{eff}) value of 8ZnS/5CdS/2TiNR indicates that it has more favorable electron-transport properties. The electron lifetime from EIS under illumination is lower than the lifetime obtained from dark EIS and OCVD owing to the more recombination paths. The larger electron density per unit volume (n_s) leads to the increased photocurrent density and solar conversion efficiency.

3.2.2. Effect of nanorods length

The J – V characteristics of typical solar cells with different nanorod length are shown in [Fig. 9](#). The open circuit potential, short circuit current density, fill factor, and energy conversion efficiency of 8ZnS/5CdS/TiNR with various titania nanorod length are listed in [Table 2](#). The cell efficiency of 8ZnS/5CdS/2TiNR is better than that of 8ZnS/5CdS/1TiNR due to the larger amount of CdS attached on the surface of 2TiNR; however, the cell efficiency with 3 μm TiNR film is poorer than that of 2 μm TiNR film. The decrease of efficiency is attributed to the obstruction of CdS nanocrystallines on the top of 3TiNR with larger diameters. The corresponding FESEM image is shown in the [supplementary information 4](#). It may lead to two explanations for the lower cell efficiency. One is that ions such as

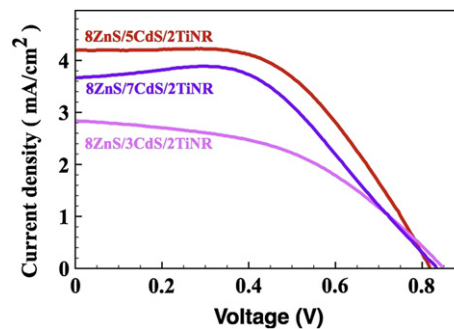


Fig. 10. Dependence of the J – V characteristics on the various CdS amounts.

Cd²⁺ and S²⁻ hardly to diffuse to the bottom of TiO₂ nanorods because of CdS rapid formation overlayer atop the TiNR as deposition of CdS. Another reason involves the electrolyte diffusion at semiconductor surfaces as photovoltaic test is being processed. It results in the interruption of hole-conducting path between electrode and electrolyte.

3.2.3. Effect of amount of CdS

[Fig. 10](#) shows the J – V characteristics of ZnS/yCdS/2TiNR. Our results exhibit that the energy conversion efficiency of photovoltaic device is enhanced by increasing CdS in increasing deposit process that leads to larger CdS nanocrystallites, which absorb a broader range of visible light. However, too much CdS deposited would reduce the efficiency (see [Supplementary information 5](#)). It might be due to the formation of a CdS overlayer atop the TiNR. In the 8ZnS/5CdS/2TiNR based solar cell device exhibits the highest efficiency with a value of 1.8%. The complete 8ZnS/5CdS/2TiNR device characteristics are as follows: $V_{\text{OC}} = 0.82$ V, $J_{\text{SC}} = 4.19$ mA cm⁻², and FF = 0.54.

4. Conclusion

In summary, we used a facile hydrothermal method to directly grow one-dimensional single crystalline rutile titania nanorods on FTO substrates. Nanocrystalline CdS was subsequently deposited onto the surface of the titania nanorods via the SILAR method to enhance absorption in the visible light region. The ZnS protection layer was coated onto the CdS/TiNR surface to prevent corrosion of the CdS nanoparticles and to facilitate photocarriers transportation to TiO₂. The short-circuit photocurrent, open circuit potential, solar conversion efficiency, and IPCE are further enhanced by deposition of ZnS passivation layer. The performance of the photoanode with ZnS was optimized by varying the lengths of the titania nanorods, the content of CdS sensitizer and the thickness of the ZnS passivation layer. The highest efficiency of 1.8% was achieved with 8ZnS/5CdS/2TiNR as a photoanode.

Acknowledgment

We acknowledge the financial support from Academia Sinica and National Science council of Taiwan.

Appendix A. Supplementary data

Supplementary data related to this article can be found at <http://dx.doi.org/10.1016/j.jpowsour.2013.01.089>.

References

- [1] M. Hoffman, S. Martin, W. Choi, D. Bahnemann, Chem. Rev. 95 (1995) 69.

Table 2
Photovoltaic performance parameters of ZnS/CdS/TiNR electrode.

Photoanodes	V_{OC} (V)	J_{SC} (mA cm ⁻²)	FF (%)	η (%)
Effect of ZnS amounts				
5CdS/2TiNR	0.75	1.72	62	0.8
2ZnS/5CdS/2TiNR	0.79	2.19	54	0.9
8ZnS/5CdS/2TiNR	0.82	4.19	52	1.8
10/ZnS/5CdS/2TiNR	0.83	2.36	62	1.0
Effect of CdS amounts				
8ZnS/3CdS/2TiNR	0.85	2.84	47	1.1
8ZnS/5CdS/2TiNR	0.82	4.19	54	1.8
8ZnS/7CdS/2TiNR	0.83	3.66	52	1.6
Effect of TiNR length				
8ZnS/5CdS/1TiNR	0.84	3.75	43	1.4
8ZnS/5CdS/2TiNR	0.82	4.19	54	1.8
8ZnS/5CdS/3TiNR	0.77	2.61	51	1.0

- [2] I.-D. Kim, A. Rothschild, B.H. Lee, D.Y. Kim, S.M. Jo, H.L. Tuller, *Nano Lett.* 6 (2006) 2009.
- [3] T. Sreethawong, T. Puangpetch, S. Chavadej, S. Yoshikawa, *J. Power Sources* 165 (2007) 861.
- [4] A. Kudo, Y. Miseki, *Chem. Soc. Rev.* 38 (2008) 253.
- [5] P. Kubiak, M. Pfanztel, J. Geserick, U. Hörmann, N. Hüsing, U. Kaiser, M. Wohlfahrt-Mehrens, *J. Power Sources* 194 (2009) 1099.
- [6] S. Ding, J.S. Chen, Z. Wang, Y.L. Cheah, S. Madhavi, X. Hu, X.W. Lou, *J. Mater. Chem.* 21 (2011) 1677.
- [7] M. Grätzel, *Inorg. Chem.* 44 (2005) 6841.
- [8] C.-J. Lin, W.-K. Tu, C.-K. Kuo, S.-H. Chien, *J. Power Sources* 196 (2011) 4865.
- [9] J.A. Chang, J.H. Rhee, S.H. Im, Y.H. Lee, H.-J. Kim, S.I. Seok, M.K. Nazeeruddin, M. Grätzel, *Nano Lett.* 10 (2010) 2609.
- [10] T.R.B. Foong, Y. Shen, X. Hu, A. Sellinger, *Adv. Funct. Mater.* 20 (2010) 1390.
- [11] J. Qiu, F. Zhuge, K. Lou, X. Li, X. Gao, X. Gan, W. Yu, H.-K. Kim, Y.-H. Hwang, *J. Mater. Chem.* 21 (2011) 5062.
- [12] G.K. Mor, K. Shankar, M. Paulose, O.K. Varghese, C.A. Grimes, *Nano Lett.* 5 (2005) 191.
- [13] H. Li, S.K. Martha, R.R. Unocic, H. Luo, S. Dai, J. Qu, *J. Power Sources* 218 (2012) 88.
- [14] K. Shankar, G.K. Mor, H.E. Prakasham, S. Yoriya, M. Paulose, O.K. Varghese, C.A. Grimes, *Nanotechnology* 18 (2007) 065707.
- [15] O.K. Varghese, M. Paulose, C.A. Grimes, *Nat. Nanotechnol.* 4 (2009) 592.
- [16] X. Feng, K. Shankar, O.K. Varghese, M. Paulose, T.J. Latempa, C.A. Grimes, *Nano Lett.* 8 (2008) 3781.
- [17] C.-J. Lin, W.-Y. Yu, Y.-T. Lu, S.-H. Chien, *Chem. Commun.* (2008) 6031.
- [18] B. Liu, E.S. Aydil, *J. Am. Chem. Soc.* 131 (2009) 3985.
- [19] M.A. Hossain, J.R. Jennings, Z.Y. Koh, Q. Wang, *ACS Nano* 5 (2011) 3172.
- [20] C.-H. Chang, Y.-L. Lee, *Appl. Phys. Lett.* 91 (2007) 053503.
- [21] H. Lee, M. Wang, P. Chen, D.R. Gamelin, S.M. Zakeeruddin, M. Grätzel, M.K. Nazeeruddin, *Nano Lett.* 9 (2009) 4221.
- [22] P. Ardalán, T.P. Brennan, H.-B.-R. Lee, J.R. Bakke, I.-K. Ding, M.D. McGehee, S.F. Bent, *ACS Nano* 5 (2011) 1495.
- [23] D.R. Baker, P.V. Kamat, *Adv. Funct. Mater.* 19 (2009) 805.
- [24] M. Li, Y. Liu, H. Wang, H. Shen, W. Zhao, H. Huang, C. Liang, *J. Appl. Phys.* 108 (2010) 094304.
- [25] Y.-L. Lee, C.-H. Chang, *J. Power Sources* 185 (2008) 584.
- [26] C.-Z. Yao, B.-H. Wei, L.-X. Meng, H. Li, Q.-J. Gong, H. Sun, H.-X. Ma, X.-H. Hu, *J. Power Sources* 207 (2012) 222.
- [27] H. Pathan, C. Lokhande, *Bull. Mater. Sci.* 27 (2004) 85.
- [28] S. Banerjee, S.K. Mohapatra, P.P. Das, M. Misra, *Chem. Mater.* 20 (2008) 6784.
- [29] W. Zhu, X. Liu, H. Liu, D. Tong, J. Yang, J. Peng, *J. Am. Chem. Soc.* 132 (2010) 12619.
- [30] L.J. Diguna, Q. Shen, J. Kobayashi, T. Toyoda, *Appl. Phys. Lett.* 91 (2007) 023116.
- [31] Y.-L. Lee, C.-F. Chi, S.-Y. Liao, *Chem. Mater.* 22 (2010) 922.
- [32] A. Braga, S. Giménez, I. Concina, A. Vomiero, I. Mora-Seró, *J. Phys. Chem. Lett.* 2 (2011) 454.
- [33] J. Bisquert, A. Zaban, M. Greenshtein, I. Mora-Seró, *J. Am. Chem. Soc.* 126 (2004) 13550–13559.
- [34] V. González-Pedro, X. Xu, I. Mora-Seró, J. Bisquert, *ACS Nano* 4 (2010) 5783–5790.
- [35] M. Adachi, M. Sakamoto, J. Jiu, Y. Ogata, S. Isoda, *J. Phys. Chem. B* 110 (2006) 13872.